ACS APPLIED MATERIALS & INTERFACES

Research Article

www.acsami.org

Electrospun Hierarchical TiO_2 Nanorods with High Porosity for Efficient Dye-Sensitized Solar Cells

Hong-Yan Chen, Teng-Long Zhang, Jie Fan, Dai-Bin Kuang,* and Cheng-Yong Su*

MOE Key Laboratory of Bioinorganic and Synthetic Chemistry, KLGHEI of Environment and Energy Chemistry, State Key Laboratory of Optoelectronic Materials and Technologies, School of Chemistry and Chemical Engineering, Sun Yat-sen University, Guangzhou, Guangdong 510275, P. R. China

Supporting Information

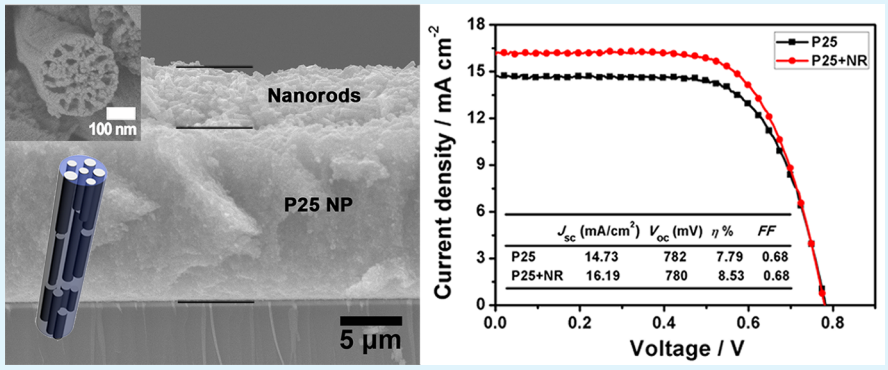

ABSTRACT: Ultraporous anatase TiO_2 nanorods with a composite structure of mesopores and macropores fabricated via a simple microemulsion electrospinning approach were first used as photoanode materials for high-efficiency dye-sensitized solar cells (DSSCs). The special multiscale porous structure was formed by using low-cost paraffin oil microemulsion droplets as the soft template, which can not only provide enhanced adsorption sites for dye molecules but also facilitate the electrolyte diffusion. The morphology, porosity, and photovoltaic and electron dynamic characteristics of the porous TiO_2 nanorod based DSSCs were investigated in detail by scanning electron microscopy (SEM), N_2 sorption measurements, current density–voltage (J–V) curves, UV–vis diffuse reflectance spectra, electrochemical impedance spectroscopy (EIS), intensity modulated photocurrent/photovoltage spectroscopy (IMPS/IMVS), and open-circuit voltage decay (OCVD) measurements. The results revealed that, although fewer amounts of dyes were anchored on the porous TiO_2 nanorod films, they exhibited stronger light scattering ability, fast electrolyte diffusion, and extended electron lifetime compared to the commercial P25 nanoparticles. A power conversion efficiency of 6.07% was obtained for the porous TiO_2 nanorod based DSSCs. Moreover, this value can be further improved to 8.53% when bilayer structured photoanode with porous TiO_2 nanorods acting as the light scattering layer was constructed. This study demonstrated that the porous TiO_2 nanorods can work as promising photoanode materials for DSSCs.

KEYWORDS: *dye-sensitized solar cells, TiO_2 nanorods, porous structure, electron lifetime, light scattering*

INTRODUCTION

As promising low-cost alternatives for solar energy conversion photovoltaic devices, dye-sensitized solar cells (DSSCs) are of enormous interest due to their relatively high photoelectric efficiency, abundant raw materials, cost-effective fabrication process, and the unique transparent devices compared to conventional silicon solar cells.[1−3] In these cells, the semiconductor photoanode is one of the key components of DSSCs since it works as both the substrate for dye adsorption and the transport path for injected electron.[4−6] To obtain a high light harvesting efficiency (LHE), an excellent photoanode should provide a large specific surface area with a large amount of adsorption sites for dye molecules; meanwhile, a strong light scattering ability is also essential to obtain an optical enhancement effect. Moreover, the semiconductor photoanode should provide a fast electron transport rate to ensure high electron collection efficiency (η_{cc}). Since the characteristics of TiO_2 photoelectrodes, including nanostructure, surface properties, and crystallinity, are crucial aspects affecting the photovoltaic performance of DSSCs, much effort has been made to optimize the microstructure of the TiO_2 photoanodes in recent years. Various TiO_2 architectures, such as nanoparticles,[1,7] one-dimensional (1D)/quasi-1D nanotubes/nanowires/nanorods,[8,9] hierarchical microspheres,[10] hollow spheres,[11−13] porous films,[14] etc.,[15] have been investigated as photoanode materials for DSSCs. Among them, hierarchical porous structures have recently attracted much attention due to the synergistic advantages of high surface area and porosity, which

Received: July 16, 2013
Accepted: August 20, 2013
Published: August 20, 2013

can not only provide abundant dye adsorption sites but also improve the electrolyte diffusion efficiency in photoanodes.

Small nanoparticle based photoanodes can provide a large specific surface area for a large amount of dye loading, but its disordered network and the presence of numerous grain boundaries reduces the electron mobility and leads to slow transport rate but strong recombination of photogenerated electrons, thus limiting the efficiency improvement.[16,17] In this context, 1D nanostructures, including nanorods, nanowires, and nanotubes, have been applied to overcome this problem.[18−20] Compared to nanoparticles, the high crystallinity, low number of grain boundaries and surface defects, and direct transport pathway for injected electrons of 1D nanostructures that largely shortens the electron transport distances can accelerate electron transport and reduce the possibility of interfacial recombination. It has been reported that the electron mobility in single crystal nanowires was about 2 orders of magnitude higher than that in nanoparticle film,[19,21] while the recombination rate in TiO_2 nanotubes was 10 times slower than that in nanoparticles.[22] However, the performances of most 1D nanostructure based DSSCs were not as high as expected due to their low surface area. Therefore, engineering the elaborate microstructure of 1D nanomaterials to provide a large specific surface area becomes a hot issue. Much attention has been paid to hierarchically structured 1D materials, including nanoforest,[23,24] nanoflowers,[25] branched nanowires,[26] etc.

Among the methods for fabricating TiO_2 fibrous materials, the electrospinning technique has become a commonly used top-down way to prepare inorganic oxide nanofibers in recent years due to its simple and low-cost fabrication process.[27,28] Furthermore, it is very easy to control the microstructure of electrospun fibers by optimizing the experimental parameters, including the structure of experimental devices[29,30] or the properties of the precursor solution;[31,32] e.g., porous nanofibers can be fabricated by introducing proper template materials into the precursor solution. In combination with post treatments, such as hot press, solvent vapor fumigation, and calcination processes, electrospun TiO_2 fibrous materials have been reported as 1D/quasi-1D photoanode materials for DSSCs.[33−35] However, the obtained conversion efficiency of electrospun TiO_2 nanofiber based cells was usually lower than 5% under AM 1.5 G illumination, mainly because of their smooth surfaces and low porosity which leads to low dye adsorption. In this regard, hierarchical porous 1D TiO_2 nanofibers with large surface areas are worthwhile to fabricate so as to pursue a higher LEH.[36,37] For example, electrospun mesoporous anatase TiO_2 nanofibers prepared by using ionic liquids as the template were reported recently to get an enhanced energy conversion efficiency of 5.64% due to their large surface area and good electron transport.[37]

In this study, ultraporous anatase TiO_2 nanorods were fabricated via a microemulsion electrospinning approach in combination with sol−gel chemistry and were used as photoanode materials for DSSCs. By using low-cost paraffin oil microemulsion droplets as the templates, hierarchical pores with a typical composite structure of mesopores and macropores were formed inside the nanorods after calcination. The features of this special multiscale porous structure include the following: (a) it provides large adsorption sites for dye molecules; (b) it facilitates electrolyte diffusion within the photoanode; (c) it helps multiply the reflecting incident light. As a result, the porous TiO_2 nanorod based DSSCs showed an energy conversion efficiency of 6.07%, which can be further improved to 8.53% when bilayer structured photoanode with porous TiO_2 nanorods acting as the light scattering layer was constructed.

EXPERIMENTAL SECTION

Preparation of Porous TiO_2 Nanofibers via the Microemulsion Electrospun Method. The porous TiO_2 nanofibers were prepared according to a previous report.[38] First, the precursor microemulsion was prepared by dissolving 0.5 g of polyvinyl pyrrolidone (PVP, M_w = 1 300 000), 0.25 g of hexadecyl trimethyl ammonium bromide (CTAB), and 3.0 g of titanium butoxide [$Ti(OBu)_4$] in a mixture of ethanol (6.5 g) and acetic acid (0.5 g) to form a homogeneous solution; subsequently, 1.5 g of paraffin oil was added under stirring, and a transparent microemulsion was obtained finally. Second, the as-prepared microemulsion was loaded into a plastic syringe equipped with a blunt stainless steel needle, and hybrid nanofibers were fabricated through an electrospinning process. The metal orifice was connected with the anode of high voltage supply, and grounded aluminum foil was used as the collector. The work distance between the orifice and collector was 20 cm, and a high voltage electric field (20−30 kV) was applied between them. After the electrospinning process, the as-prepared hybrid fibers were calcined at 500 °C for 2 h to obtain porous TiO_2 nanofibers.

Preparation of TiO_2 Nanorod Photoanodes. The porous TiO_2 nanorod photoanodes were prepared through a well-developed screen-printing method.[39] The as-synthesized TiO_2 nanofibers were grinded with a certain amount of absolute ethanol, ethyl cellulose, acetic acid, and terpineol to form a viscous slurry paste. Then, the paste was screen-printed onto the surface of FTO glass (15 Ω/square, Nippon Sheet Glass, Japan) to obtain homogeneous films, which were calcined further in a muffle furnace to remove the organic compounds. The programmed temperature process was 325 °C for 5 min, 375 °C for 5 min, 450 °C for 15 min, 500 °C for 15 min, and then cooled naturally. The film thickness was controlled by repeating the printing process and was measured by a profilometer (Ambios, XP-1). For comparison, commercial P25 nanoparticle photoanodes with similar thickness were also prepared via the same screen-printing process. In order to improve the connection between particles, the as-prepared TiO_2 photoanodes were soaked in 0.04 M $TiCl_4$ aqueous solution for 30 min at 70 °C, first, and sintered at 520 °C for 30 min. Then, the photoanode films were immerged into N719 dye solution (0.5 mM in acetonitrile/*tert*-butanol mix−solvent, volume ratio 1:1) and sensitized for about 16 h at room temperature. Finally, the dye-sensitized films were rinsed with acetonitrile to remove the physisorption dye molecules and dried in air. The active area of the TiO_2 photoanode was approximately 0.16 cm^2 which was accurately determined by a profilometer before each measurement.

Assembly of DSSCs Devices and Characterizations. To assemble the devices, the dye-sensitized photoanodes were fastened together with the platinized counter electrodes to form simple cells. Before the fasten process, a drop of I^-/I_3^- redox pair based liquid electrolyte containing 0.03 M I_2, 0.05 M LiI, 0.6 M 1-methyl-3-propylimidazolium iodide (PMII), 0.10 M guanidinium thiocyanate, and 0.5 M tertbutylpyridine in a mixture of acetonitrile/valeronitrile (85:15, volume ratio) was dripped onto the photoanode. The platinized counter electrodes were fabricated by thermal depositing isopropanol solution of 5 mM chloroplatinic acid (H_2PtCl_6) onto the surface of FTO glass substrate at 400 °C for 15 min.

The morphology and structure of the porous TiO_2 nanofibers and TiO_2 nanorod photoanodes were examined by X-ray diffractometry (XRD, D-MAX 2200 VPC) and field emission scanning electron microscopy (FE-SEM, JSM-6330F). The specific surface area and pore size distribution of porous TiO_2 nanofibers was determined through N_2 sorption measurements by using an ASAP 2010 surface area analyzer (Micrometritics Instrument Corporation). The diffuse reflectance of photoanode films and dye amounts attached on the film was measured by UV−vis diffuse reflectance spectra and absorption spectra, respectively, on a UV−vis-NIR spectrophotometer (Shimadzu UV-3150).

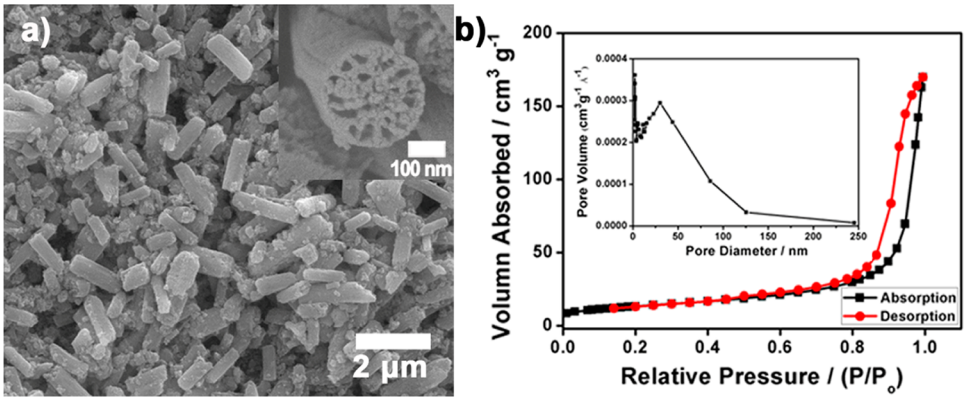

Figure 1. (a) Top SEM image of porous TiO_2 nanorod photoanode film; inset: magnified cross-section image of a single nanorod showing the hierarchical pore structures. (b) N_2 adsorption−desorption isotherms of porous TiO_2 nanofibers prepared from the microemulsion electrospinning method; inset: the corresponding calculated pore-size distribution plot.

The current density−voltage (J−V) characteristics of DSSCs were recorded by a Keithley 2400 source meter. The cells were illuminated by a solar light simulator (Oriel, Model: 91192) equipped with a 1000 W xenon arc lamp (Oriel, Model: 6271) or tested in the dark, and the incident light intensity was set as one sun AM 1.5 G 100 mW cm^{-2}, which was calibrated by a NREL-calibrated Si solar cell before each measurement. An electrochemical workstation (Zahner Zennium) was used to record the electrochemical impedance spectroscopy (EIS). The measurements were carried out in the dark at a bias potential of open-circuit voltage with the frequency ranging from 10 mHz to 1 MHz, and the magnitude of the alternative signal was 10 mV. The electron transport time and electron lifetime were measured by intensity-modulated photocurrent spectroscopy (IMPS) and intensity-modulated photovoltage spectroscopy (IMVS). The measurements were also performed on the same Zahner electrochemical workstation equipped with a frequency response analyzer. An intensity modulated blue light emitting diode (457 nm) driven by a source supply (Zahner, PP211) was used as the light source. The light intensity was set as 30, 60, 90, 120, and 150 W m^{-2}, respectively, and the scanning frequency range was between 1000 Hz and 100 mHz. The modulated light intensity was 10% or less than the base light intensity.

RESULTS AND DISCUSSION

Hierarchical porous TiO_2 nanofibers with high porosity were fabricated through the microemulsion electrospinning method in combine with sol−gel chemistry. This method features of the microemulsion electrospun solution in which $Ti(OBu)_4$ worked as the consecutive phase and the precursor of TiO_2 while paraffin oil droplets worked as the dispersion phase as well as the pore-forming soft template. Through the electrospun process, hybrid nanofibers with paraffin oil encapsulated in the solid amorphous Ti−O−Ti network were obtained, and anatase TiO_2 porous nanofibers were prepared by a subsequent calcination treatment to remove the organics. The pores corresponding to the vacancies of oil droplets were formed after their removal from fibers.[38] Figures 1 and S1, Supporting Information, show the morphology and pore structure of as-prepared fibers. The diameter of fibers ranges from tens of nanometers to ∼800 nm (Figure S1, Supporting Information). The cross section of the fibers (Figure 1a, inset) clearly shows a porous structure inside the fiber with pore diameter ranging from several nanometers to tens of nanometers. It was proposed that this special pore structure can be attributed to: (i) the partial demulsification of small paraffin oil droplets to form bigger ones due to the rapid solvent evaporation and the hydrolysis condensation of metal alkoxide in the instant electrohydrodynamic process; (ii) the quick elongation of the charged liquid during the electrospun process driven by the strong electric field forces and the bending instability. That is the merged paraffin oil droplets with different size induced the formation of multiscale porous structure.[38] Nitrogen-adsorption measurements of the samples (Figure 1b) give a Brunauer−Emmett−Teller (BET) surface area of 47.8 m^2 g^{-1}, and a characteristic hysteresis loop at higher relative pressures can be observed in the plot, indicating the presence of mesopores. Moreover, as determined by the Barrett−Joyner−Halenda (BJH) adsorption method calculated from the absorption isotherms, the maximum pore size distribution of the pore is around 30 nm with a relatively broad size distribution (Figure 1b, inset), showing a typical composite structure of macropores and mesopores. This multiscale porous structure of nanofibers would be of great benefit to the dye loading and electrolyte filtration when working as photoanode materials for DSSC.

To characterize the photoelectrical performance of the multiscale porous nanofibers, the samples were grinded into nanorods and screen-printed onto the surface of FTO glass to form photoanode films. As shown in Figure 1a, the photoanode film consists of nanorods with length smaller than ∼2 μm. Some small nanoparticles exist between them which should be generated from the crushed nanofibers during the grinding process. Compared with long nanofibers, the short nanorods can greatly enhance the effective specific surface area of films because many close pores encapsulated in fibers became exposed in the short rods, which can greatly enhance the dye loading and facilitate the electrolyte diffusion in photoanode. For comparison, commercial P25 nanoparticle based photoanodes (denoted as Cell P25) with the same thickness as the porous nanorod photoanodes (denoted as Cell NR) were also prepared. Figure 2 and Table 1 show the photocurrent density−voltage (J−V) curves of the DSSCs based on different photoanodes and the corresponding photovoltaic parameters calculated from the curves, including short-circuit current density (J_{sc}), open-circuit voltage (V_{oc}), fill factor (FF), and conversion efficiency (η). The J_{sc} of Cell NR is 11.16 mA cm^{-2}, a little lower than that of Cell P25 (13.65 mA cm^{-2}). The lower J_{sc} should be attributed to lower dye loading of the nanorod photoanode resulting from its lower specific surface area (47.8 vs. 59.9 m^2 g^{-1} for P25 nanoparticles). According to the UV−vis absorption spectra of solutions containing dyes detached from the photoanodes, the saturated dye adsorption of porous nanorod film was calculated to be 86.8 nmol cm^{-2}, while the

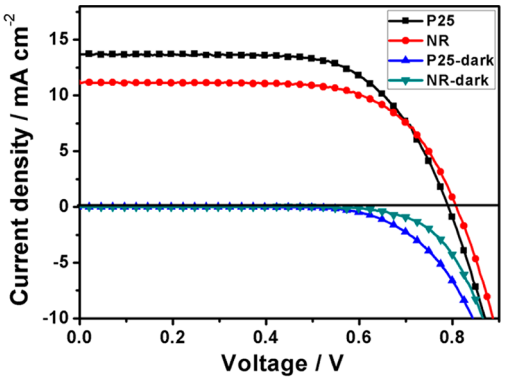

Figure 2. Photocurrent–voltage curves (top) and dark current–voltage curves (down) of DSSCs based on P25 nanoparticle film and porous nanorod film, respectively.

Table 1. Photovoltaic Parameters of Different Photoanode Based DSSCs Measured under AM 1.5 G Full Sunlight Illumination (100 mW cm^{-2})

photoanode	thickness/ μm	dye adsorption/ nmol cm^{-2}	J_{sc}/ mA cm^{-2}	V_{oc}/ mV	η/%	FF
NR	15	86.8	11.16	808	6.07	0.67
P25	15	136.6	13.65	791	7.11	0.66
P25	20	164.8	14.73	782	7.79	0.68
P25 + NR	20	146.5	16.19	780	8.53	0.68

value for P25 film was 136.6 nmol cm^{-2}. Therefore, a lower photogenerated current density was predictable. However, as far as the ratio of J_{sc} to dye amounts anchored on photoanode was concerned, the value of Cell NR (0.13) was higher than that of Cell P25 (0.10). This may be attributed to the stronger light scattering ability and excellent electron transport properties of 1D nanorods. In addition, the V_{oc} of Cell NR (808 mV) is higher than that of Cell P25 (791 mV), which should result from the slower electron recombination in the former cell. As shown in Figure 2, the dark current density of Cell P25 is much higher than Cell NR since its onset, indicating a serious electron recombination reaction existing in the former cell. On the contrary to the case of light illumination, electrons were injected into the cell through the TiO_2 photoanode to reduce the I_3^- in electrolyte and the resulting I^- was oxidized at the counter electrode when tested in the dark. Therefore, a higher dark current density in cells indicated more serious recombination reaction happening at the interface between photoanode and electrolyte.[39] The lower electron recombination rate in Cell NR can be further confirmed by electrochemical impedance spectroscopy (EIS) and intensity modulated photocurrent spectroscopy/photovoltage spectroscopy (IMPS/IMVS) measurements as discussed below. As a result, the porous nanorod photoanode based cell exhibited a conversion efficiency of 6.07%, a little lower than the value obtained by P25 nanoparticle photoanode.

The light scattering ability of porous nanorod photoelectrode was characterized by the UV–vis diffused reflectance spectra. Since the size of nanorods was comparable to the wavelength of visible and near-infrared light, a strong light scattering ability can be expected. Moreover, the highly porous structure with hierarchical macrospores and mesopores inside nanorods may also help multiply the reflecting and scattering incident light, which will effectively enhance the optical pathway of incident light. As shown in Figure 3, the porous nanorod photoanode film shows a strong light reflectance over the whole visible

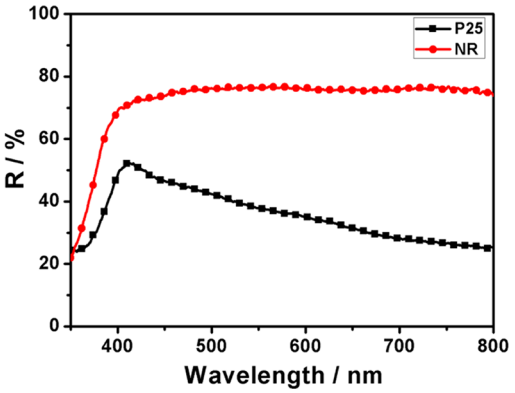

Figure 3. Diffused reflectance spectra of porous nanorod and P25 photoanodes without dye loading, respectively, showing the strong light scattering effect of nanorod photoanode.

range of 400–800 nm; moreover, the value is as high as above 70%. In contrast, the reflectance of P25 film is lower, especially in the long wavelength range. The high scattering effect of porous nanorods will definitely increase the light harvesting efficiency of photoanode film, thus leading to an enhanced photocurrent density for the DSSCs.

To further explore the influences of the properties of nanorod photoanode on the performance of corresponding DSSCs, EIS measurements were carried out. Figure 4 shows the

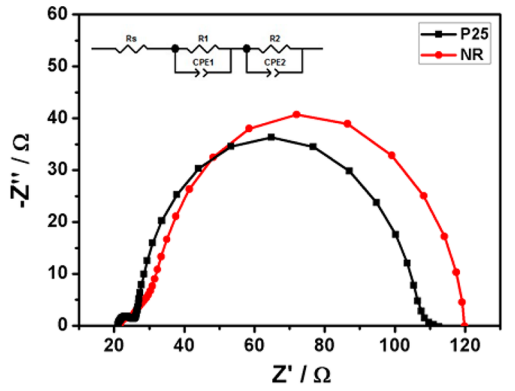

Figure 4. Nyquist plots of cells composed of porous nanorod and P25 nanoparticle photoanode measured in the dark at forward bias of open-circuit voltage. Inset is the equivalent circuit used to fit the plots by Z-view software.

Nyquist plots of the two cells measured at a forward bias of open-circuit voltage in the dark. Two semicircles, including a small one at higher frequency and a large one at lower frequency, are observed in the plots. The small semicircle can be assigned to the charge-transfer resistance (R_1) and the capacitance (C_1) at the Pt counter electrode/redox electrolyte interface, while the larger semicircle is ascribed to the recombination resistance (R_2) and chemical capacitance (C_2) at the TiO_2/dye/redox electrolyte interface.[40,41] According to the fitting results obtained by Z-view software using an equivalent circuit containing resistance (R) and constant phase element (CPE) (Figure 4, inset), the electron recombine resistance (R_2) of Cell NR is calculated to be 88.4 Ω, a little higher than the value of Cell P25 (79.3 Ω), which indicates a

dx.doi.org/10.1021/am402853q | ACS Appl. Mater. Interfaces 2013, 5, 9205–9211

slower electron recombination process for the former cell. The electron lifetime estimated by $\tau = R_2 \times CPE_2$ of Cell NR (91.0 ms) is much higher than that of Cell P25 (63.7 ms). As we have known, a longer electron lifetime will lead to a higher V_{oc}, and this result is in accordance with the $J-V$ data.

The electron transport and charge recombination of the DSSCs based on different photoanodes were further characterized by IMPS and IMVS measurements. The electron transport time can be estimated from the relation $\tau_d = 1/2\pi f_{IMPS}$, where f_{IMPS} is the characteristic frequency of the minimum IMPS imaginary component; the electron lifetime (or recombination time) was determined using the relation $\tau_r = 1/2\pi f_{IMVS}$, where f_{IMVS} is the characteristic frequency of the minimum IMVS imaginary component.[33,42] Figure 5 shows the

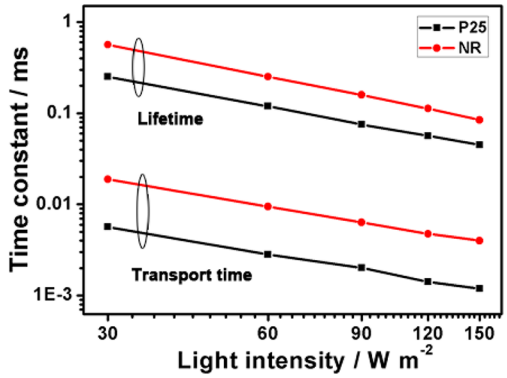

Figure 5. Incident light intensity dependent transport time and lifetime constants in porous TiO_2 nanorods and P25 nanoparticle based cells.

τ_d and τ_r as a function of incident light intensity, which is 30, 60, 90, 120, and 150 W m^{-2}, respectively. It is clear that both the electron transport time and the lifetime decrease with increasing light intensity, but the Cell NR exhibits both longer electron transport time and longer electron lifetime than Cell P25 under various light intensities, indicating a slower electron transport rate but a longer electron lifetime in the former cell. The longer electron lifetime in Cell NR can be attributed to fewer grain boundaries and thus fewer trapping sites for the photogenerated electrons in the porous nanorod film, which can accelerate the electron transport to a certain extent and also effectively reduce the electron recombination reaction. As we know, the electron transport in nanoparticle films occurs via a trap-limited diffusion process, and the serious electron recombination reaction caused by a large amount of grain boundaries, defects, and surface states, which can act as electron trapping sites, is a key point that limits the photoelectric performance of the nanoparticle based photoanode.[16] Compared with P25 films, the relatively defect free quasi-1D porous nanorod films have fewer grain boundaries and the connectivity between nanoparticles is enhanced, which results in fewer electron trapping events at particle–particle interfaces; thereby, a longer electron lifetime can be expected. Furthermore, as mentioned before, the dark $J-V$ characteristics of Cell NR (Figure 2) also showed a lower dark current than that for Cell P25; this is consistent with the fewer back reactions and slower recombination for nanorod based cells. The longer electron lifetime in Cell NR further confirmed its higher V_{oc}. However, the electron transport rate in porous nanorod film is lower, which should be mainly due to the fact that the dye loading of porous TiO_2 nanorod film is lower than that of P25 nanoparticle film due to its smaller specific surface area than the latter, which would result in a lower photocurrent density and thus a lower electron density gradient and a longer electron transport time. In addition, differing from the aligned 1D nanostructures arrays, which always provide a direct electron transport path to accelerate the electron transport,[9,18] the photogenerated electrons walk randomly in many cases in the unordered quasi-1D nanorod film, which may lead to a slow electron transport rate. These results indicate that the porous nanorods can work as promising photoanode materials for DSSCs.

Furthermore, the electron recombination kinetics in different photoanode based cells was characterized by open-circuit voltage-decay (OCVD) measurement in which the transient V_{oc} as a function of time since switching off the incident light was investigated.[43−45] As shown in Figure 6a, the V_{oc} decays

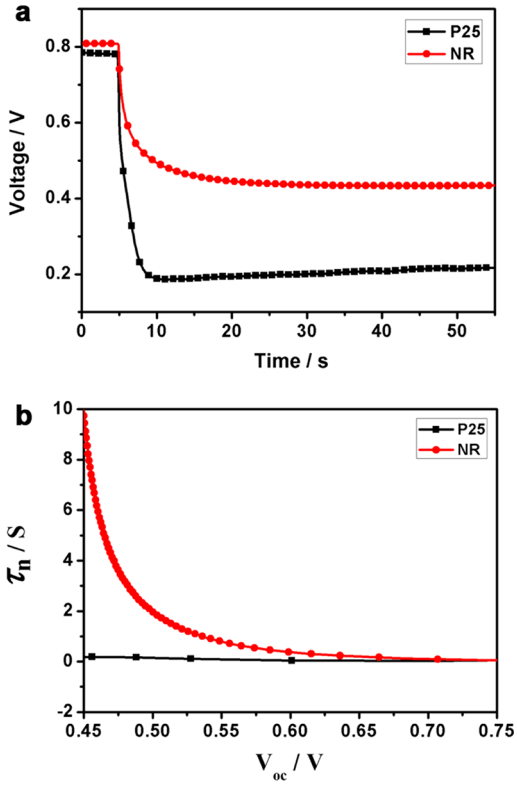

Figure 6. (a) Comparison of open-circuit voltage-decay curves between DSSCs based on P25 and nanorod photoanodes. (b) The calculated electron lifetime from curves in (a).

dramatically after the illumination is switched off because of electron recombination, but the voltage decay rate in Cell NR is much slower than Cell P25, which means the back electron recombination reaction between electrons in the conduction band of TiO_2 with oxidative species in electrolyte can be effectively inhibited and a longer electron lifetime was obtained in the former cell. Furthermore, the lifetime of photogenerated electrons (τ_n), which is calculated by the equation of $\tau_n = -(k_BT/e)(dV_{oc}/dt)^{-1}$, where k_B is the Boltzmann constant and T is the temperature, is shown in Figure 6b. It is evident that τ_n of Cell NR is longer than that of Cell P25. This result is in good agreement with the EIS, IMPS, and IMVS studies shown above.

All these results demonstrate that the hierarchical porous nanorods can work as good candidates for efficient photoanode

materials of DSSCs due to their enhanced dye loading, strong light scattering ability, and excellent electron transport performance. Therefore, a bilayer structured photoanode with hierarchical porous nanorod film as light scattering layer and P25 nanoparticle film as the dye adsorption layer was constructed (Figure 7a) so as to further improve the conversion

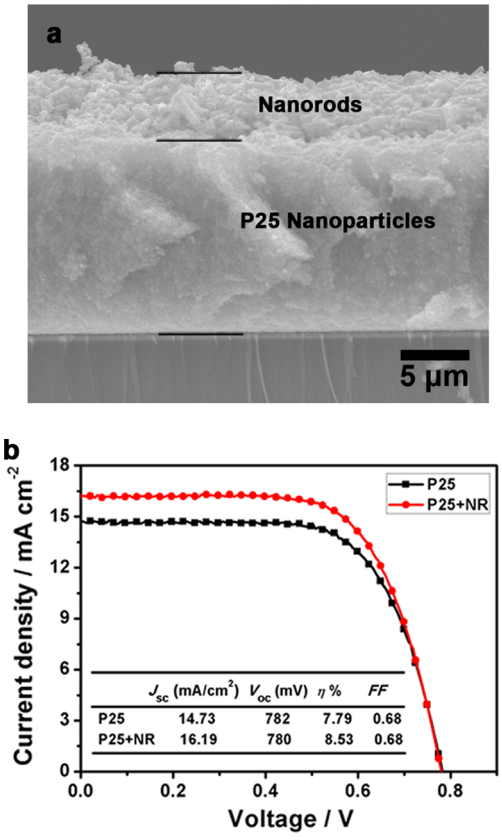

Figure 7. (a) Cross section SEM image of bilayer structured photoanode with P25 nanoparticle bottom layer and porous nanorods top layer. (b) Comparison between $J-V$ curves of cells based on the bilayer photoanode and single-layer P25 photoanode with the same thickness.

efficiency of DSSCs. Figure 7b shows the comparison between $J-V$ curves of cells based on the bilayer photoanode with about 15 μm of P25 bottom layer and 5 μm of nanorod top layer (Cell P25+NR) and the single-layer P25 photoanode with the similar thickness. For the single-layer P25 photoanode, it exhibits a little higher J_{sc} of 14.73 mA cm^{-2} than the 15 μm photoanode due to its increased dye adsorption (164.8 nmol cm^{-2}); however, the V_{oc} is decreased to 782 mV due to the more serious electron recombination in the thicker photoanode film. Thereby, an overall conversion efficiency of 7.79% is obtained. Compared with P25 film, the J_{sc} of bilayer structure photoanode based cell is much higher (16.19 mA cm^{-2}), although its dye adsorption amount (146.5 nmol cm^{-2}) is a little lower. This can be attributed to the strong light scattering ability of hierarchical porous nanorods which effectively enhanced the light harvesting efficiency of bilayer structured photoanode. As a result, a higher conversion efficiency of as high as 8.53% is obtained, which is 9.5% higher than that of a single-layer P25 film. This result further indicates that the hierarchical porous nanorods synthesized via the micro-emulsion electrospinning method can work as excellent photoanode materials for DSSCs.

CONCLUSION

In summary, hierarchical porous TiO_2 nanorods prepared via a simple microemulsion electrospinning method were used as efficient photoanode materials for DSSCs. By using paraffin oil microemulsion droplets as the soft template and a subsequent calcination process after electrospinning, multiscale porous anatase nanofibers were obtained. When used as photoanode materials for DSSCs, the quasi-1D nanorod film exhibited strong light scattering ability, longer electron lifetime, and fast electrolyte diffusion efficiency compared to the commercial P25 nanoparticles, which was confirmed by UV−vis diffuse reflectance spectra, EIS, IMPS/IMVS, and OCVD measurements. As a result, the porous nanorod based DSSCs showed a significant power conversion efficiency of 6.07%, which can be further improved to 8.53% when the porous nanorods were used as light scattering layer to construct bilayer structured photoelectrode, indicating the excellent photovoltaic performance of porous nanorods. Moreover, the porous nanorods reported here may also show great potential in working as efficient photoanode materials for quasi-solid/solid-state DSSCs, since the composite pore structure of nanorods is big enough to facilitate the electrolyte diffusion in photoanode forming good ohm contact between them, especially for the viscous quasi-solid/solid-state electrolyte.

ASSOCIATED CONTENT

Supporting Information

Additional SEM image of porous TiO_2 nanofibers. This information is available free of charge via the Internet at http://pubs.acs.org/.

AUTHOR INFORMATION

Corresponding Authors

*E-mail: kuangdb@mail.sysu.edu.cn. Fax: 86-20-8411-3015. Tel: 86-20-8411-3015.

*E-mail: cesscy@mail.sysu.edu.cn. Fax: 86-20-8411-3015. Tel: 86-20-8411-3015

Notes

The authors declare no competing financial interest.

ACKNOWLEDGMENTS

The authors acknowledge the financial support from the National Natural Science Foundation of China (201103236, U0934003), the Program for New Century Excellent Talents in University (NCET-11-0533), the Fundamental Research Funds for the Central Universities, Guangdong Natural Science Foundation (S2011040001464), the China Postdoctoral Science Foundation funded project (Grant No. 201104374), and the Research Fund for the Doctoral Program of Higher Education (20100171110014, 20110171120026).

REFERENCES

(1) O'Regan, B.; Grätzel, M. *Nature* **1991**, *353*, 737−740.

(2) Hagfeldt, A.; Boschloo, G.; Sun, L. C.; Kloo, L.; Pettersson, H. *Chem. Rev.* **2010**, *110*, 6595−6663.

(3) Yella, A.; Lee, H.-W.; Tsao, H. N.; Yi, C.; Chandiran, A. K.; Nazeeruddin, M. K.; Diau, E. W.-G.; Yeh, C.-Y.; Zakeeruddin, S. M.; Grätzel, M. *Science* **2011**, *334*, 629−634.

(4) Zhang, Q. F.; Cao, G. Z. *Nano Today* **2011**, *6*, 91−109.

(5) Chen, H.-Y.; Kuang, D.-B.; Su, C.-Y. *J. Mater. Chem.* **2012**, *22*, 15475−15489.
(6) Zhang, Q. F.; Cao, G. Z. *J. Mater. Chem.* **2011**, *21*, 6769−6774.
(7) Chou, T. P.; Zhang, Q.; Russo, B.; Fryxell, G. E.; Cao, G. *J. Phys. Chem. C* **2007**, *111*, 6296−6302.
(8) Feng, X.; Shankar, K.; Varghese, O. K.; Paulose, M.; Latempa, T. J.; Grimes, C. A. *Nano Lett.* **2008**, *8*, 3781−3786.
(9) Mor, G. K.; Shankar, K.; Paulose, M.; Varghese, O. K.; Grimes, C. A. *Nano Lett.* **2005**, *6*, 215−218.
(10) Kim, Y. J.; Lee, M. H.; Kim, H. J.; Lim, G.; Choi, Y. S.; Park, N. G.; Kim, K.; Lee, W. I. *Adv. Mater.* **2009**, *21*, 3668−3673.
(11) Lai, X.; Halpert, J. E.; Wang, D. *Energy Environ. Sci.* **2012**, *5*, 5604−5618.
(12) Du, J.; Qi, J.; Wang, D.; Tang, Z. *Energy Environ. Sci.* **2012**, *5*, 6914−6918.
(13) Dong, Z.; Lai, X.; Halpert, J. E.; Yang, N.; Yi, L.; Zhai, J.; Wang, D.; Tang, Z.; Jiang, L. *Adv. Mater.* **2012**, *24*, 1046−1049.
(14) Cho, C.-Y.; Moon, J. H. *Adv. Mater.* **2011**, *23*, 2971−2975.
(15) Yang, N.; Yuan, Q.; Zhai, J.; Wei, T.; Wang, D.; Jiang, L. *ChemSusChem* **2012**, *5*, 572−576.
(16) Berger, T.; Lana-Villarreal, T.; Monllor-Satoca, D.; Gómez, R. *J. Phys. Chem. C* **2007**, *111*, 9936−9942.
(17) van de Lagemaat, J.; Park, N. G.; Frank, A. J. *J. Phys. Chem. B* **2000**, *104*, 2044−2052.
(18) Zhu, K.; Neale, N. R.; Miedaner, A.; Frank, A. J. *Nano Lett.* **2007**, *7*, 69−74.
(19) Law, M.; Greene, L. E.; Johnson, J. C.; Saykally, R.; Yang, P. D. *Nat. Mater.* **2005**, *4*, 455−459.
(20) Jennings, J. R.; Ghicov, A.; Peter, L. M.; Schmuki, P.; Walker, A. B. *J. Am. Chem. Soc.* **2008**, *130*, 13364−13372.
(21) Forro, L.; Chauvet, O.; Emin, D.; Zuppiroli, L.; Berger, H.; Lévy, F. *J. Appl. Phys.* **1994**, *75*, 633−635.
(22) Zhu, K.; Neale, N. R.; Miedaner, A.; Frank, A. J. *Nano Lett.* **2006**, *7*, 69−74.
(23) Sauvage, F.; Di Fonzo, F.; Bassi, A. L.; Casari, C. S.; Russo, V.; Divitini, G.; Ducati, C.; Bottani, C. E.; Comte, P.; Grätzel, M. *Nano Lett.* **2010**, *10*, 2562−2567.
(24) Ghosh, R.; Brennaman, M. K.; Uher, T.; Ok, M.-R.; Samulski, E. T.; McNeil, L. E.; Meyer, T. J.; Lopez, R. *ACS Appl. Mater. Interfaces* **2011**, *3*, 3929−3935.
(25) Jiang, C. Y.; Sun, X. W.; Lo, G. Q.; Kwong, D. L.; Wang, J. X. *Appl. Phys. Lett.* **2007**, *90*, 263501.
(26) Liao, J.-Y.; Lei, B.-X.; Chen, H.-Y.; Kuang, D.-B.; Su, C.-Y. *Energy Environ. Sci.* **2012**, *5*, 5750−5757.
(27) Greiner, A.; Wendorff, J. H. *Angew. Chem., Int. Ed.* **2007**, *46*, 5670−5703.
(28) Li, D.; Xia, Y. *Adv. Mater.* **2004**, *16*, 1151−1170.
(29) Chen, H.; Wang, N.; Di, J.; Zhao, Y.; Song, Y.; Jiang, L. *Langmuir* **2010**, *26*, 11291−11296.
(30) Zhao, Y.; Cao, X. Y.; Jiang, L. *J. Am. Chem. Soc.* **2007**, *129*, 764−765.
(31) Bognitzki, M.; Czado, W.; Frese, T.; Schaper, A.; Hellwig, M.; Steinhart, M.; Greiner, A.; Wendorff, J. H. *Adv. Mater.* **2001**, *13*, 70−72.
(32) Xu, X. L.; Zhuang, X. L.; Chen, X. S.; Wang, X. R.; Yang, L. X.; Jing, X. B. *Macromol. Rapid Commun.* **2006**, *27*, 1637−1642.
(33) Lee, B. H.; Song, M. Y.; Jang, S. Y.; Jo, S. M.; Kwak, S. Y.; Kim, D. Y. *J. Phys. Chem. C* **2009**, *113*, 21453−21457.
(34) Fujihara, K.; Kumar, A.; Jose, R.; Ramakrishna, S.; Uchida, S. *Nanotechnology* **2007**, *18*, 365709.
(35) Song, M. Y.; Kim, D. K.; Ihn, K. J.; Jo, S. M.; Kim, D. Y. *Nanotechnology* **2004**, *15*, 1861−1865.
(36) Hwang, S. H.; Kim, C.; Song, H.; Son, S.; Jang, J. *ACS Appl. Mater. Interfaces* **2012**, *4*, 5287−5292.
(37) Lin, Y. P.; Chen, Y. Y.; Lee, Y. C.; Chen-Yang, Y. W. *J. Phys. Chem. C* **2012**, *116*, 13003−13012.
(38) Chen, H.; Di, J.; Wang, N.; Dong, H.; Wu, J.; Zhao, Y.; Yu, J.; Jiang, L. *Small* **2011**, *7*, 1779−1783.
(39) Chen, H.-Y.; Liao, J.-Y.; Lei, B.-X.; Kuang, D.-B.; Fang, Y.; Su, C.-Y. *Chem. Asian J.* **2012**, 1795−1802.
(40) Wang, Q.; Ito, S.; Grätzel, M.; Fabregat-Santiago, F.; Mora-Seró, I.; Bisquert, J.; Bessho, T.; Imai, H. *J. Phys. Chem. B* **2006**, *110*, 25210−25221.
(41) Fabregat-Santiago, F.; Bisquert, J.; Palomares, E.; Otero, L.; Kuang, D.; Zakeeruddin, S. M.; Grätzel, M. *J. Phys. Chem. C* **2007**, *111*, 6550−6560.
(42) Dloczik, L.; Ileperuma, O.; Lauermann, I.; Peter, L. M.; Ponomarev, E. A.; Redmond, G.; Shaw, N. J.; Uhlendorf, I. *J. Phys. Chem. B* **1997**, *101*, 10281−10289.
(43) Zaban, A.; Greenshtein, M.; Bisquert, J. *ChemPhysChem* **2003**, *4*, 859−864.
(44) Xu, C.; Shin, P. H.; Cao, L.; Wu, J.; Gao, D. *Chem. Mater.* **2009**, *22*, 143−148.
(45) Wu, W.-Q.; Liao, J.-Y.; Chen, H.-Y.; Yu, X.-Y.; Su, C.-Y.; Kuang, D.-B. *J. Mater. Chem.* **2012**, *22*, 18057−18062.